Highly Textured CMOS-compatible Hexagonal Boron Nitride-based Neuristor for Reservoir Computing

Haizhong Zhang[1], Jiayi Li[2], Xin Ju[3]*, Jie Jiang[4], Jing Wu[3], Dongzhi Chi[3], Diing Shenp Ang[2], Wei Hu[1], Rongshan Wei[1], Minmin Zhu[1]*, and Xiaoqiang Lu[1]

[1]College of Physics and Information Engineering, Fuzhou University, Fuzhou, China, 350116;

[2]Nanyang Technological University, Singapore, 639798;

[3]Institute of Materials research and Engineering, 2 Fusionopolis Way, Innovis, #08-03, Agency for Science, Technology and Research, Singapore, 138634;

[4]Hunan Key Laboratory of Nanophotonics and Devices, School of Physics, Central South University, 932 South Lushan Road, Changsha, Hunan 410083, P. R. China

*Corresponding authors.

E-mail: ju_xin@imre.a-star.edu.sg; mmzhu@fzu.edu.cn

ABSTRACT

Significant advancements in artificial neural networks (ANNs) have driven the rapid progress of artificial intelligence and machine learning. While current feedforward neural networks primarily handle static data, recurrent neural networks (RNNs) are designed for dynamical systems. However, RNNs demand extensive training on specific tasks, limiting their scalability and affordability for edge computing. Physical reservoir computing (RC) offers an alternative approach by mapping inputs into high-dimensional states, allowing for pattern analysis within a fixed reservoir. Unlike RNNs, RC is well-suited for temporal and sequential data processing with rapid speed and low training costs. This makes RC suitable for hardware implementation across various research domains. Nonetheless, existing demonstrations of RC remain constrained to small-scale device arrays. As electronic synapse arrays aim to approach very large-scale and highly complex hardware as in the human brain, managing heat dissipation becomes a formidable challenge. In this work, we successfully developed the neuristors based on textured h-BN films, prepared using a CMOS-compatible technique, and constructed a physical RC system based on as-fabricated devices. Our approach leverages vertically aligned BN to provide aligned diffusion paths for the reproducible migration process of metal ions from the electrodes and offers a potential solution for thermal management in electronic devices. This achievement highlights the promising potential of our neuristors for future high-density and energy-efficient neuromorphic computing.

Keywords: Boron nitride; Highly textured; High thermal conductivity; Neuromorphic device; Reservoir computing;

1. Introduction

Conventional artificial neural networks (ANNs), emulating biological neural networks with interconnected processing units and weighted links, [1–8] have made remarkable strides in the fields of artificial intelligence and machine learning. These ANNs can be categorized into feedforward neural networks, which handle static data processing, and recurrent neural networks (RNNs), tailored for dynamic data processing due to their capacity to incorporate temporal dependencies. However, RNNs often necessitate extensive, task-specific training, making them unsuitable for edge computing and therefore demand faster physical processing units and more efficient algorithms. In recent times, physical reservoir computing (RC) as an alternative brain-inspired framework has garnered growing interest across various research domains, [9-12] Derived from RNN models, RC comprises a fixed reservoir that maps inputs into a high-dimensional space and a trainable readout for pattern analysis. Unlike traditional RNNs, RC excels in temporal and sequential data processing, while offering rapid learning capabilities with minimal training cost. Its non-adaptive reservoir allows for hardware implementation using diverse physical systems, substrates, and devices.

Despite the potential of RC, current implementations are typically constrained to small-scale device arrays. As electronic synapse arrays aim to approach the complexity of the human neural network, the management of heat dissipation emerges as a formidable challenge. This thermal challenge not only limits energy efficiency but also impedes the integration of very large-scale and highly complex hardware as in the human brain. Hexagonal boron nitride (h-BN) is characterized by planar hexagonal networks, held together by covalent B-N bonding and weak van der Waals forces.[13–16] It possesses a range of intriguing properties, including a wide bandgap in the 5.6 eV to 6.5 eV range,[17] high in-plane thermal conductivity,[18] exceptional mechanical strength, and robust UV photoluminescence.[19,20] Compared to conventional oxides, h-BN can be produced with a very smooth and even surface, significantly minimizing device fluctuations. Additionally, h-BN has excellent chemical stability, preventing interactions with neighbouring layers. Unlike other 2D conducting and semiconducting materials, h-BN can fabricate memristor devices without requiring a transfer process (i.e., direct growth on metal substrates). These properties highlight the promise of h-BN for neuromorphic computing. In particular, vertically aligned h-BN, where the c-axis aligns with the substrate surface, offers a promising solution to address thermal hotspots in electronic devices. Its high thermal conductivity has been under investigation for use as a heat-spreader in AlGaN/GaN high electron mobility transistors (HEMTs), as described in our prior work,[21] where efficient heat dissipation is vital for preserving high electronic mobility. The development of electronic synapses based on high-quality growth h-BN thin films holds the potential for realizing large-scale and high-performance memory, and neuromorphic computing applications in the future.

While several deposition techniques for hexagonal boron nitride (h-BN) are available, such as chemical vapor deposition, pulse laser deposition, and radio frequency (RF) magnetron sputtering,[22–24] the challenge of mass-producing high-quality aligned h-BN films persists. This challenge is primarily attributed to the substantial B-N binding energy and the low atomic weight of boron and nitrogen. Among the CMOS-compatible methods, RF magnetron sputtering appears promising due to the dielectric properties of both h-BN and pure boron.[25] However, it has many drawbacks, including low ionization, low sputtered material density, and susceptibility to radio interference. To address these limitations, high power impulse magnetron sputtering (HIPIMS) emerges as a favorable fabrication technique for h-BN. As a type of pulsed magnetron sputtering, HIPIMS offers distinct advantages, including high ion densities and target power during the sputtering process.[26] Moreover, HIPIMS permits precise manipulation of parameters such as duty cycle, pulse on-time, and pulse frequency, providing new avenues for controlling the microstructure of h-BN thin films.

In this study, we successfully achieved highly textured h-BN on a flexible copper foil substrate using HIPIMS technique. We then developed a physical RC system based on fabricated two-terminal h-BN neuristors. The vertical alignment of BN effectively facilitates copper ion dynamics, ensuring reservoirs with excellent separation and echo state characteristics (i.e., possessing intrinsic nonlinearity and time-dependent response). The applicability of the proposed device is verified by demonstrating the RC system for classifying fashion images. Good classification performance metrics are showcased with an accuracy of 95% and great robustness to noise corruption of the input data. These findings demonstrate the potential use of our devices in real-time, energy-efficient neuromorphic computing systems.

2. Results and discussion

Our study replicates biological synapses using a highly textured h-BN-based memristor, composed of a vertically stacked Au/BN/CuO/Cu structure **(Fig. 1a)**. The top electrode (TE) serves as the presynaptic input, and the bottom electrode (BE) serves as the postsynaptic output.

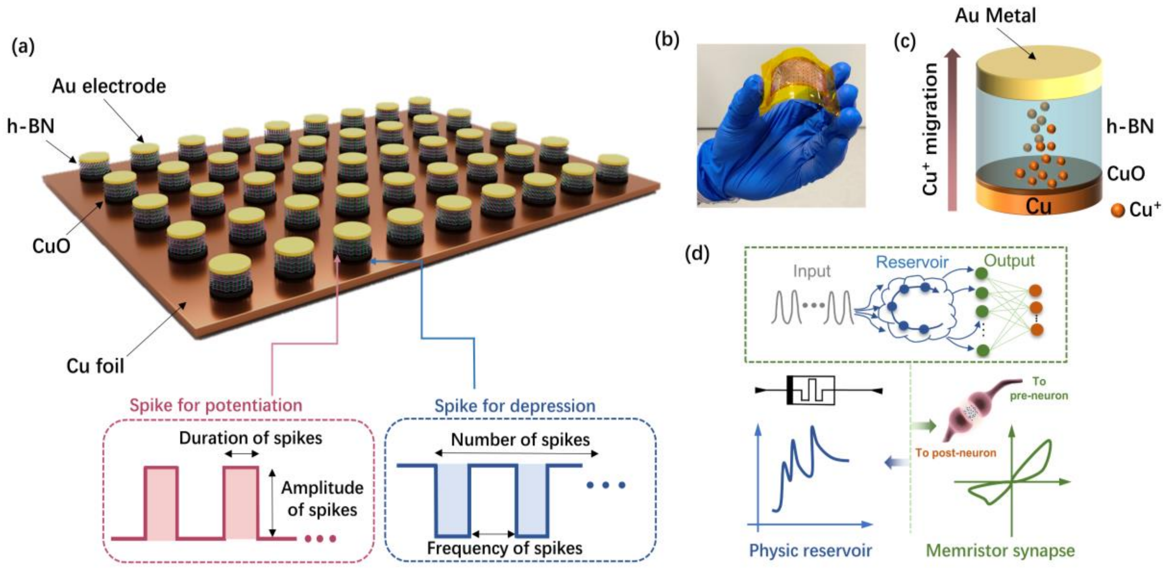

Figure 1. (a) Schematic of a synaptic memristor array with an Au/h-BN/CuO/Cu device structure. The device exhibits spike-dependent learning capabilities for both potentiation and depression. (b) Photograph of a flexible BN-based synaptic device array. (c) 3D schematic of the Au/BN/CuO/Cu stacked structure device and its operation under electrical stimulation. (d) Proposed dynamic BN memristor-based reservoir computing (RC) system. The diagram within the dashed box represents the abstract RC system. Raw electrical data is initially processed in a physical reservoir, where inputs undergo nonlinear mapping, generating feature outputs through the paired-pulse facilitation (PPF) effect. These outputs are then received by a memristor synapse array, which undergoes readout training.

We experimentally demonstrate synaptic characteristics under varying spiking conditions, involving two voltage spiking conditions (one for potentiation and the other for depression) with varying parameters such as the number, amplitude, duration, and frequency of pulses. These findings highlight the device's potential for computational tasks, including signal processing and image recognition. In **Fig. 1b**, we present a photograph of an h-BN memristor array fabricated on copper foil, emphasizing its flexibility and bendable nature. The device achieves reversible formation and rupture of conductive filaments (CFs) through redox and ionic migration processes involving reactive metal cations (Cu^{2+}), leading to resistance changes (**Fig. 1c**). The reservoir computing (RC) system comprises a reservoir layer and an output readout layer, outlined in **Fig. 1d**. Within this RC system, the states in the reservoir layer are nonlinearly mapped by temporal inputs and are correlated with their previous states.[27–29] The weights in the readout layer are fine-tuned for specific learning tasks, and the ultimate outputs are typically derived from a linearly weighted combination of feature outputs from the reservoir layer.[30,31] The pair-pulsed facilitation effect with tunable nonlinear properties makes the

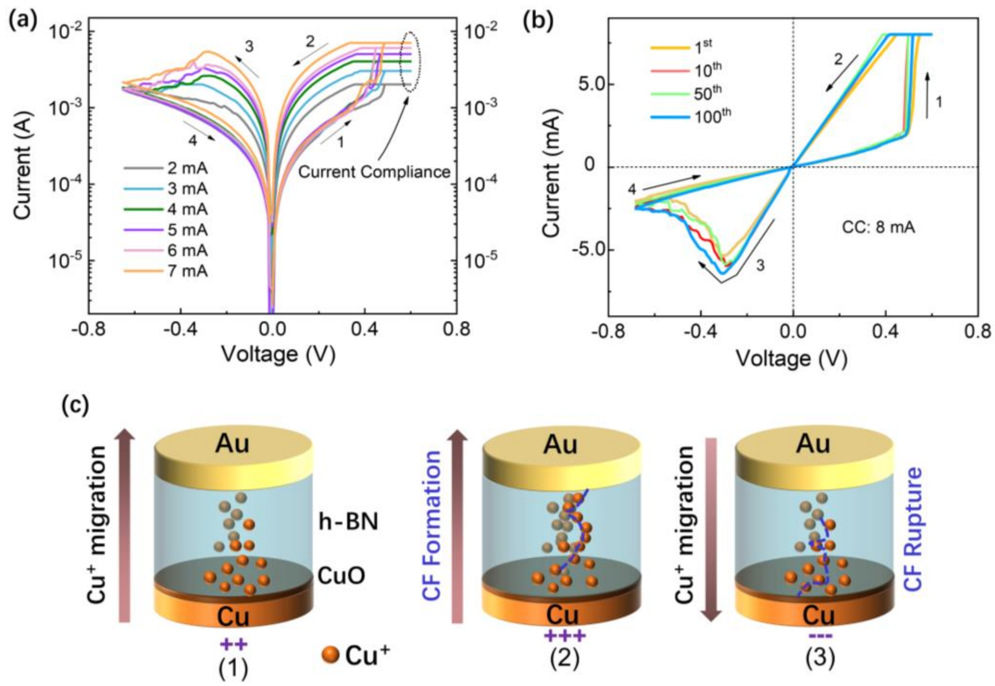

Figure 2. (a) Schematic diagram of typical biological synapse, and (b) Electronic synapse based on Au/BN/CuO/Cu device stack structure. (c) Principle diagram of the resistive switching mechanism of Au/BN/CuO/Cu devices.

device ideal for use as physical reservoirs. Additionally, their adjustable resistive state characteristics are well-suited for use as readout layers, naturally performing vector-matrix multiplications in the array structure.

Fig. 2a illustrates the electrical response of our h-BN-based neuromorphic device to varying current compliances (CC). During measurements, we directly applied an external voltage bias to the Cu electrodes, keeping the Au electrode grounded. A notable feature is the absence of a forming process for resistive switching. Specifically, our electronic synapse transitions from a high resistance state (HRS) to a low resistance state (LRS) as the external voltage varies from 0 to +0.6 V during set switching. It subsequently returns to HRS (reset switching) as the voltage is varied from 0 to −0.6 V. These tunable resistance states are pivotal for emulating the potentiation and depression behaviors observed in bio-synapses of neural systems. It is interesting that multiple switchable resistance states can be obtained by adjusting the CC level. This characteristic demonstrates the capability to manipulate the conductance of electronic synapses between LRS and HRS, a crucial feature for information storage and potential applications in neuromorphic computing. We further showcase the device's ability to repeatedly switch resistance under a CC of 8 mA (**Fig. 2b**), underscoring its reliability and applicability in real-world scenarios. The ON and OFF cycles of the device showed excellent operational stability after 100 cycles (**Fig.S1**), although some minor fluctuations were observed.

The resistive switching in our Au/BN/CuO/Cu sandwiched structure is attributed to the creation of a conductive channel composed of Cu filaments (**Fig. 2c**). When the external electric field approaches the breakdown electric field of the CuO layer, typically situated between the BN film and the Cu substrate, Cu-O bond dissociation periodically occurs (Step 1). Cu ions are released from the CuO layer and drift toward the Au electrode under the applied bias. Simultaneously, lateral outward drift of oxygen anions transpires, resulting in a sharp surge in current along the Cu-rich breakdown path (Step 2). As the current approaches the preset CC limit, the analyzer promptly intervenes to maintain compliance with the prescribed limit. This is accompanied by the effect of Joule heating, which mitigates undesirable structural changes. Upon reversing the negative voltage sweep, Cu ions are directed back into the conductive path (Step 3). This process leads to the creation of a gap within the breakdown path, inducing an increase in resistance during the breakdown process, effecting the transition from a state of low resistance to high resistance (e.g., a reset process). Therefore, the conductance, or synaptic weight, of the synapse can be finely adjusted by controlling the formation and dissolution of a conductive filament within the synaptic-like gap, contingent on the change in external voltage polarity. This dynamic modulation mechanism holds significance for neuromorphic applications.

The presence of the CuO layer plays a crucial role in the switching behavior of h-BN-based electronic synapses. We utilized high-resolution transmission electron microscopy (HRTEM) to examine the interface between the h-BN layer and the copper substrate, confirming the existence of a thin CuO interfacial layer of 1 nm between the BN film and the Cu substrate (**Fig. 3a).** HRTEM images of the h-BN and copper regions demonstrate the good crystallinity of both Cu and h-BN **(Fig. 3b** and **3c**). HRTEM analysis further verifies the successful acquisition of highly textured h-BN, indicated by the presence of discontinuous diffraction rings in the selected area electron diffraction (SAED) pattern (Inset of **Fig. 3b**).[26,32] It is worth noting that the highly textured h-BN film exhibits approximately 354% higher thermal conductivity compared to its randomly oriented counterpart (Supporting information, **Table S1**). **Fig. S2a** and **2b** show the absorbance spectra of the random (sample A) and highly textured (sample B) h-BN films, respectively. It can be concluded that the optical band gaps of samples A and B are 5.33 eV and 5.77 eV, respectively. Furthermore, to compare the heat dissipation effect and its stability at high temperatures, the thermal conductivities of the two samples were measured at different temperatures. The thermal conductivity of sample B was always higher than that of sample A and remained relatively constant throughout the temperature range, with a difference of 25% from the average value. These properties indicate the potential of vertically aligned h-BN for realizing high-density electronic devices with good thermal conductivity. Notably, the SAED pattern at the interface exhibits two distinct diffraction patterns (**Fig. 3d**). One is indexed as [101] Cu (white), while the other corresponds to [311] CuO (red), consistent with previous findings in CuO/Cu nanowires.[33] These results underscore the significant role of the CuO layer in the functionality of our electronic synapse.

In pursuit of robust neuristor characteristics, we examined the potential of our device for fundamental synaptic applications through electrical modulation. In human neural network, external stimulation triggers the activation of voltage-controlled Ca^{2+} channels, initiating the release of neurotransmitters from the presynaptic neuron to the receptors of the postsynaptic neuron for signal transmission.[5,34] These processes mirror the learning and memory functions, which involve the modification of synaptic connections and the adjustment of weights within

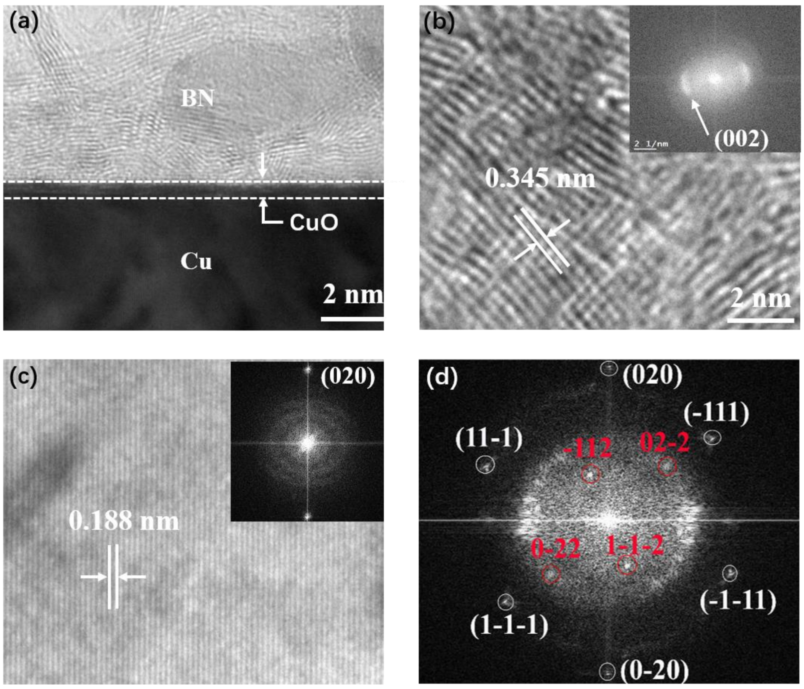

Figure 3. (a) Cross-sectional TEM image displaying the structural composition of the Au/BN/CuO/Cu device stack. HRTEM image of (b) the h-BN zone and (c) the copper zone. The insets in (b) and (c) feature the corresponding SAED patterns. (d) The SAED pattern captured at the interface between the h-BN film and the copper substrate.

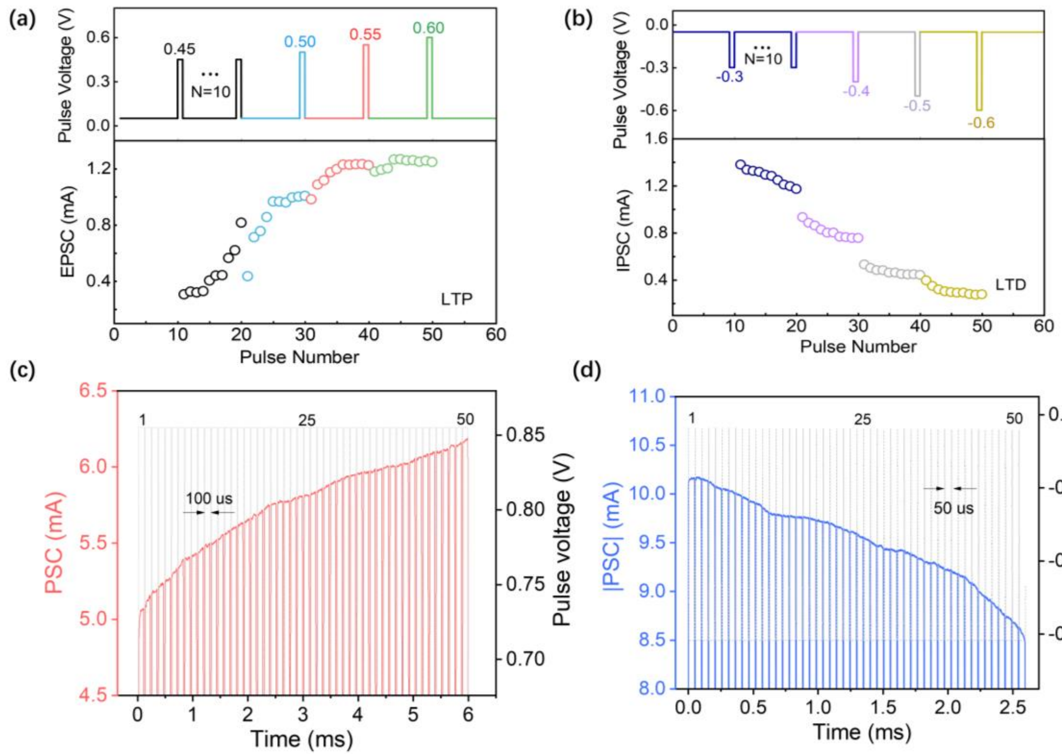

Figure 4. Electrical stimulated synaptic plasticity. (a) and (b) Excitatory/inhibitory postsynaptic currents (EPSC/IPSC) were generated by applying 10 consecutive input spikes at different voltage amplitudes with the pulse width set to 10 ms. (c) Gradual increase in conductance with continuous training pulses (V_P = +0.85 V, Δt = 100 μs) measured in real time. (d) Gradual decrease in conductance with continuous training pulses (V_D = −0.6 V, Δt = 50 μs) measured in real time.

neural networks. These memory functions can be broadly categorized into two fundamental behaviors: short-term memory (STM) and long-term memory (LTM).[35] STM is characterized by transient fluctuations in synaptic weights, while LTM represents more enduring changes that can persist from milliseconds to minutes. **Fig. S3** demonstrates the short-term plasticity after applying a 0.3 V pulse voltage for 1 ms. Moreover, an increase in training intensity can lead to more lasting weight changes through consolidation. In **Fig. 4a** and **4b**, we investigate the response behavior of the BN-based neuristor under various electrical pulsed stimuli. Gradually increased or decreased conductance, corresponding to potentiation or depression, is observed as the pulse voltage is adjusted within the range of +0.45 to +0.6 V or −0.3 to −0.6 V, with a pulse width of 10 ms and voltage step of +50 mV or −50 mV. The pulse amplitude increment leads to the migration of additional Cu^+ ions from the bottom electrode to the BN layer, resulting in the accumulation of a larger conductive bridge between the two electrodes.

Fig. 4c and **4d** demonstrate the application of successive short pulses for potentiation (V_P = +0.85 V, Δt = 100 μs) and depression (V_D = −0.6 V, Δt = 50 μs) on the device. This showcases the device's capability to achieve a continuously adjustable conductance with the presence of 50 discernible LTM states. The number of voltage pulses serves as distinct instances of training and learning. In training experiments, additional pulses lead to a larger post-synaptic current (PSC), akin to the principles of reinforcement learning.[4,36,37] The quantity of pulses can induce a transition from STM to LTM, as more metal ions are mobilized, enhancing storage performance.

The synaptic plasticity of our device was further evaluated by subjecting it to ten successive identical pulses with a pulse width and interval of 10 ms. The stability of these weight states was assessed through a 30-cycle potentiation and depression process, as illustrated in **Fig. 5a**. This test confirmed the high reproducibility of the device's ability to simulate synaptic weight regulation. The voltage amplitude of the applied pulse trains was set to +0.6 V and −0.6 V for

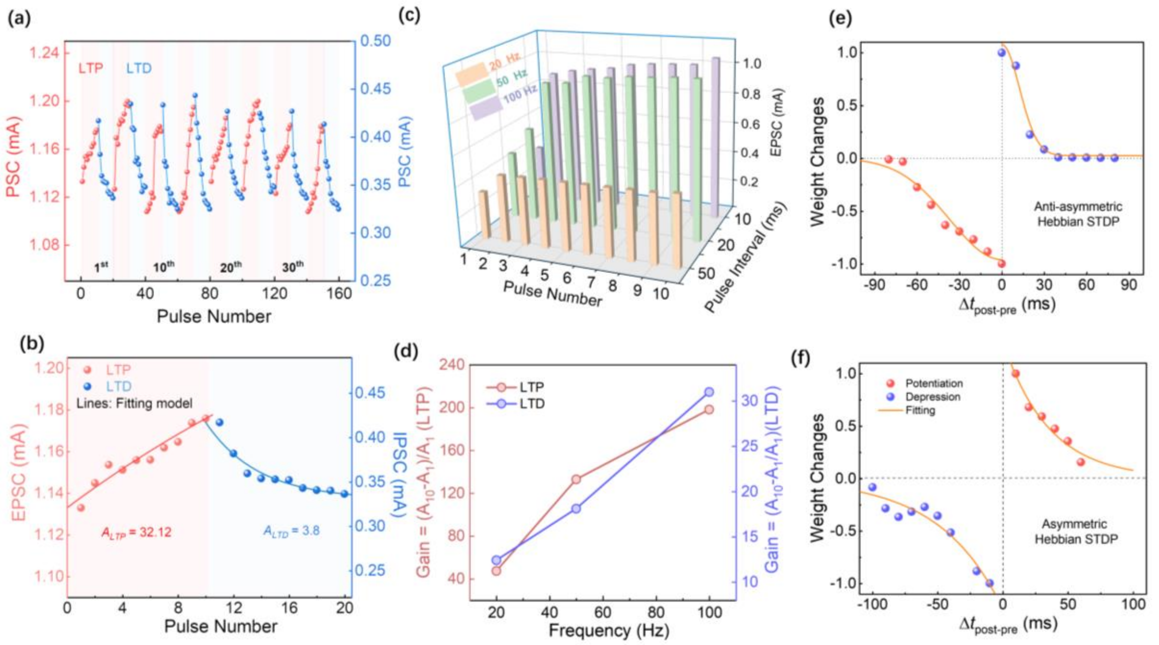

Figure 5. (a) Progressive excitatory and inhibitory PSC modulation is achieved with spike voltages (±0.6 V and 10 ms) corresponding to LTP and LTD simulations. Stable LTP/LTD synaptic properties show small cycle-to-cycle variations over 30 cycles. (b) PSC per pulse number (10 positive and 10 negative pulses). The fitting model values for potentiation and depression were found to be $A_{LTP} = 32$ and $A_{LTD} = 3.8$. (c) Current response to ten identical stimulation pulses (0.4 V, 10 ms) at different frequencies (20, 50, and 100 Hz). (d) SRDP index (defined as $(A_{10}-A_1)/A_1 \times 100\%$) versus pulse frequencies. The device is connected to two pulse sources that act as neurons for spike timing-dependent plasticity (STDP). (e) Symmetric and (f) Asymmetric STDP Hebbian learning rule.

potentiation and depression, respectively. The formation and dissolution of conducting filaments within the synaptic-like gap were precisely controlled by changing the polarity of the external voltage, thus modulating synaptic conductance (synaptic weight). Crucially, the PSC of a synapse could be finely tuned when subjected to positive or negative voltage pulses. Sequences of positive and negative pulses induced a continuous increase or decrease in conductance, demonstrating the device's capacity to emulate the long-term potentiation (LTP) and depression (LTD) activity seen in biological synapses. In **Fig. 5b**, we extracted the nonlinearity index from the PSC variation with pulse number using the following equations:[38]

$$I_{LTP} = B\left(1 - e^{-P/A}\right) + I_{min} \tag{1}$$

$$I_{LTD} = -B\left(1 - e^{-(P-P_{max})/A}\right) + I_{max} \tag{2}$$

$$B = \frac{I_{max} - I_{min}}{1 - e^{-P_{max}/A}} \tag{3}$$

where $I_{\mathrm{LTP(LTD)}}$ represents the PSC values of the LTP and LTD regions, P and $P_{\max}$ are the number of applied voltage pulses and the maximum number of pulses, respectively. A is the parameter characterizing the nonlinear behavior of the weight update, and B is the prefactor used for normalizing the current range. Efficient and precise neuromorphic operations often require good linearity.[39] The extracted LTP nonlinearity (|NL|) is 0.15, and the LTD nonlinearity is 3.2, with performance comparable to or exceeding that of other related memristive synaptic devices.[40-43] The good symmetry brings the potential for high computational performance.

Leveraging the unique inherent dynamics of our neuronic device, we also demonstrated the phenomenon of paired-pulse facilitation (PPF), which holds significant importance in neuroscience for decoding temporal visual or auditory signals using a dual-pulse programming approach.[2,44,45] PPF refers to synaptic events triggered by two consecutive electrical pulses, wherein the PSC peak triggered by the second pulse is notably larger than that of the first pulse, as shown in **Fig. S4a**. PSCs were measured after 10 ms of electrical pulses and stabilization with varying pulse intervals of 0 s, 0.2 s, and 0.5 s. It was evident that the PSC triggered after the second pre-synaptic pulse consistently exceeded that after the first pulse, with the current difference diminishing with increasing time interval. Similar behavior was observed in paired-pulse depression (PPD), as displayed in **Fig. S4b**. When a pair of voltage spikes (−0.6 V, 10 ms) was applied, the PSC triggered after the second pre-synaptic spike was significantly smaller than that following the first pre-synaptic spike.

We now delve into the spike-dependent learning capability of our synapse, with the aim of achieving bio-realistic neural networks. The human brain employs history-dependent learning rules, such as spike-rate-dependent plasticity (SRDP) and spike-timing-dependent plasticity (STDP), which we have successfully emulated in our designed synapses. SRDP is a persistent change in synaptic responsiveness to frequent synaptic activation. Learning rules adjust synaptic weights based on the presynaptic firing rate: high-frequency presynaptic pulse sequences increase synaptic strength. In **Fig. 5c**, we present the excitatory current response across three distinct frequency groups (20, 50, 100 Hz), each with a fixed 10 ms pulse duration, representing variations in applied interval based on pulse frequency. Each frequency condition involved ten consecutive stimulation spikes (0.4 V). After ten pulses, the PSC increased by 0.15, 0.58 and 0.71 mA, corresponding to 20, 50 and 100 Hz pulse frequencies, respectively. Notably, a higher pulse rate resulted in a more significant increase in PSC, and synaptic connections are tight, producing similarity to dynamic filtering (high pass filtering of signals) characteristics in biological systems. This enhancement is quantified through the gain of synaptic currents (SRDP index: $(A_{10} - A_1) / A_1 \times 100\%$), as depicted in **Fig. 5d**. Furthermore, **Fig. S5** illustrates SRDP during the depression process. These synaptic cells with history-dependent learning capabilities offer a simple and efficient operational scheme for hardware neural networks, as they can be trained without the complexity of engineering input signal pulses. In biological neural networks, spike-timing-dependent plasticity (STDP) plays a crucial role in Hebbian learning rules.[46,47] The behavior of STDP enables the modulation of synaptic weights based on the relative timing of pre- and postsynaptic spikes. This time is denoted by Δt ($\Delta t = t_{post} - t_{pre}$), where t_{pre} represents the arrival time of the pre-synaptic neuron spike and t_{post} signifies the arrival time of the post-synaptic neuron spike. Here, we have demonstrated the STDP synaptic learning rule using spike waveforms, wherein the relative spike timing between pre- and post-synaptic neurons translates into a modulation of the voltage drop across the BN-based synapse. When $\Delta t > 0$, the net effect of spike pairs is positive, inducing long-term potentiation and increasing synaptic weights, and vice versa, and the change in weight decreases with increasing $|\Delta t|$. That is, closer spikes in the time domain result in larger voltage drops, leading to more significant conductivity changes in the device. The symmetric and asymmetric STDP patterns in terms of weight changes are illustrated in **Fig. 5e** and **5f**, and they are fitted well with an exponential decay curve. The details of the pulse waveform design used to characterize the STDP characteristics are explained in **Fig. S6**. These findings underscore the capacity of our device to mimic bio-realistic neural network behavior, presenting a significant step forward in neuromorphic engineering.

Emerging neuristor holds tremendous potential for deep neural network acceleration, in-memory neuromorphic computing, and physical reservoir computing, etc.[48–51] Leveraging the excellent ion dynamics of our fabricated BN neuristors, we capitalize on the fading memory effect and inherent nonlinear properties of these devices to create reservoirs with good separation and echo state characteristics. In this study, we present a physical RC system built upon our devices, which effectively mitigates software and hardware overhead in image classification tasks. Moreover, it significantly enhances the speed of data processing, making it particularly appealing for real-time and low-energy application scenarios. Although not developed for benchmarking the physical RC system, we calculated the Kernel Rank (KR),[52] Generalisation Rank (GR),[52] and Memory Capacity (MC)[53] of our PRC system. Specifically, KR measures the linear independence of the internal states of the reservoir in response to a given set of input signals, which indicates the ability of the reservoir to map inputs to a high-dimensional space in which linear separation is easier. A higher KR suggests that the reservoir can effectively differentiate between different inputs. GR assesses the ability of the reservoir to generalize from the input data to the output tasks. It shows how well the reservoir can handle unseen data based on its training. A higher GR indicates better generalization capabilities. MC quantifies the reservoir's ability to retain and use past input information. It is a measure of how well the system can recall previous inputs, which is crucial for tasks that require temporal dependencies and context, such as time series prediction and sequence classification. Higher MC means the reservoir can remember more past inputs effectively. In our system, KR = 4, GR = 0.55, MC = 0.42.

To further validate the ability of the physical RC system to nonlinearly map simulated input information on an as-fabricated reservoir, we conducted image recognition using the Fashion-MNIST (f-MNIST) dataset.[54] As depicted in **Fig. 6a**, the system comprises an input layer that simultaneously feeds image data into the physical reservoir (PR) using electrical voltage pulses. The physical RC outputs are subsequently processed by an iteratively trained readout layer for f-MNIST dataset classification, ensuring the network achieves a relatively stable level of accuracy. The nonlinear correlation between different reservoir states, generated at specific times, is a result of the spontaneous partial rupture of the conducting filaments formed by active metal ions in our device. **Fig. 6b** displays the response output current after each predefined interval for a series of 3-bit pulse patterns. Each state represents the presence ("1") or absence ("0") of a voltage pulse stimulus. After completing the final interval, all 8 states arising from the 3-bit pulse patterns are clearly distinguishable. In **Fig. 6c**, the simulated PR outputs of a typical "Ankle Boot" image from the f-MNIST dataset is presented under different device noise rates. To account for device noise and variability, we assumed that each current output follows

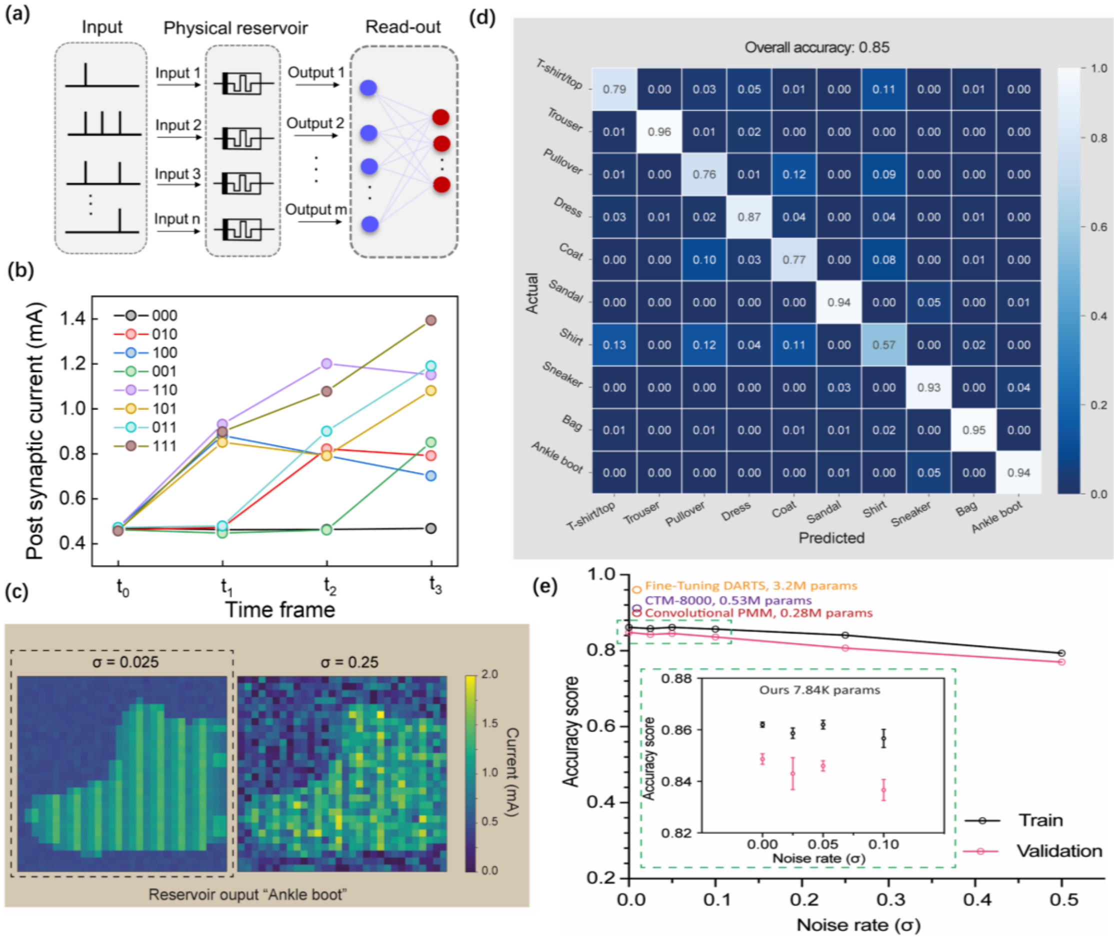

Figure. 6 (a) Schematic working principle of the proposed BN memristor-based reservoir computing (RC) system for image classification. Here, the reservoir layer is an array of BN-based memristor (simulated). The readout layer contains ten output neurons (corresponding to the ten classes of the f-MNIST dataset) and 7,840 synapses. (b) The dynamic response of the memristor to a sequence of pulses with different pulse intervals, i.e., the average physical reservoir response of the 3-bit electrical pulse read. Here, "1" indicates the arrival of a voltage pulse with an amplitude of +0.7 V and a duration of 100 μs, and "0" indicates the absence of a voltage stimulus. (c) Mapping of an example image of reservoir output with device noise and variations. (d) Confusion matrix for all 10 classes in the f-MNIST dataset showing the classification results. (e) Overall accuracy as a function of device noise rate and standard deviation of variability σ (assuming Gaussian distribution). Inset: σ has an accuracy of up to 0.1. The line shows the mean value, and the error bars indicate one standard deviation.

a Gaussian distribution with a pre-specified standard deviation, denoted as σ. For our experiments, we used 60,000 images from the f-MNIST dataset for training and reserved 10,000 samples for testing the classification accuracy of the proposed physical RC system (σ = 0.025). The results, as shown in the confusion matrix classification (**Fig. 6d**), indicate an overall accuracy of 85% for all 10 classes in the f-MNIST dataset. This demonstrates that the PR system can effectively classify various types of images, with particular success in categories such as boots, bags, and sneakers, where the accuracy reached 95%. Compared to other physical reservoir recognition accuracies (83% to 88.8%), [55-58] the accuracy of BN is similar or marginally higher (**Fig. S7**), suggesting the effectiveness of the proposed neuristors. **Fig. 6e** illustrates the overall accuracy as a function of σ. Even with a relatively high σ of 0.5, the accuracy remains at approximately 80%, confirming the robustness of the system to device noise and variability. The error bar in the inset of **Fig. 6e** further highlights minimal variation between cycles of different simulation runs. These results emphasize that the memristor-based reservoir can efficiently extract feature information from the input dataset, ultimately reducing network complexity and training costs. While memristive synaptic devices hold a bright future in reservoir computing, several technical challenges remain. The reliability and integration of the devices are of concern, with insufficient integration leading to a lack of accuracy in recognizing complicated information. Furthermore, high device integration inevitably leads to increased energy consumption and is influenced by the degree of nonlinear memory decay in the device. Long-term stability is also an important indicator of whether a memristive synaptic device can be used as a physical reservoir device.

3. Conclusions

In summary, this study presents a neuromorphic analogue implementation of RC using h-BN-based neuristors. The thermal conductivity of highly textured h-BN, fabricated through high power impulse magnetron sputtering (HIPIMS), is approximately four times greater than its randomly oriented counterpart. Our device effectively mimics typical synaptic plasticity, both excitatory and inhibitory, by analogue modulating conductance. This modulation is achieved through the control of conductive filaments formed by copper ions. Additionally, we successfully replicate key features of the biological nervous system, including recognition and decoding, frequency selection, and significant activity-dependent plasticity. Fading effect enable well-separated responses to different temporal inputs, as well as non-volatile memory switching qualifies it as synapses in readout networks. Building upon this, we have developed a physical RC system characterized by robust noise immunity and an outstanding classification accuracy of 95%. Our findings suggest that h-BN-based neuristors hold attractive promise for the development of reservoir computing systems and will stimulate further research for a new era of practical applications in this field.

4. Experimental Section

Device fabrication. Highly textured h-BN thin films were synthesized on copper substrates using HIPIMS technique. The sputtering process employed a pure boron target with an exceptional boron purity of 99.9% by mass. Before each deposition, the chamber's base pressure was meticulously reduced to below 4×10^{-6} Torr, while the substrate temperature was elevated to 800°C. Subsequently, a mixture of Ar and N_2 gases was introduced into the chamber. The characteristic pulse length of this waveform averaged around 100 μs, with a voltage applied of up to 1000 V across the target, resulting in a power density of approximately 100 $W\cdot cm^{-2}$. Finally, a 60 nm-thick Au electrode was deposited onto the BN/CuO/Cu structure using electron-beam deposition, thus completing the formation of the Au/BN/CuO/Cu device.

Characterization and device measurement. The detailed microstructure of the samples was investigated using a JEOL 2100F TEM equipped with a Schottky field emission gun, operating at 200 kV. X-ray diffraction analysis was conducted using a Shimadzu XRD-6000 machine, employing Cu Kα radiation (λ = 0.15418 nm) to examine the phase information and crystallinity of the samples. To assess the bonding characteristics of the as-synthesized BN thin films, X-ray photoelectron spectroscopy (XPS) was performed using an argon ion sputter gun and an Al Ka X-ray energized source with a photon energy of 1486.6 eV. For electrical characterization, DC and pulsed voltage-sweep testing were carried out at room temperature utilizing a Keithley SCS4200/Agilent B1500A parameter analyzer. The semiconductor parameter analyzer was connected to the bottom electrode (Cu) through Au-coated tungsten probes.

Simulation. A customized physical reservoir (PR) computing simulation platform was built. The pulse train pattern of 0.6 V amplitude and 10 ms duration was used to stimulate the reservoir node (h-BN neuristors). A fully connected readout layer was used for classifying the simulated neuristors reservoir output, which was offline supervised trained with logistic regression (maximum-entropy classification) by stochastic average gradient (SAG) solver with L1 regularization. Fashion MNIST dataset containing 70,000 images of fashion styles categorised into 10 classes was used for benchmarking the simulated PR system, where 60,000 was used for training and the rest 10,000 separated images was saved for validation. The static image was input into the dynamic PR row by row, with a simulated reset every 3 pixels. Each run in the simulation was independent. All simulation programs were exploit in Python 3.9 environment.

ASSOCIATED CONTENT

Author Information

X.J., H.Z.Z. proposed the collaboration and performed the measurement, M.M.Z. fabricated the devices, H.Z.Z., J.Y.L., X.J., J.J., J.W., D.Z.C., D. S. A., W.H., R.S.W., X.Q.L. and M.M.Z. carried out the analysis, X.J., H.Z.Z., and M.M.Z. designed the experiments. J.Y.L., X.J., and D.S.A. conceived the idea and carried out the simulation. All authors contributed to the preparation of the manuscript.

Corresponding Author

*Email: ju_xin@imre.a-star.edu.sg; mmzhu@fzu.edu.cn

ACKNOWLEDGEMENTS

This work is supported by National Natural Science Foundation of China (Grant No. 62274036), National Research Foundation Competitive Research Program, Singapore (NRF-CRP24-2020-0002).

STATEMENTS AND DECLARATIONS

Competing Interests: The authors declare no competing financial interest.

Supplementary Information

The following files are available free of charge. The properties comparison of highly textured and random structure of BN film, endurance behavior of the device, the synaptic plasticity of paired-pulse facilitation and depression, and the spike-rate-dependent plasticity during the depression process.

References

[1] W. Zhang, P. Yao, B. Gao, Q. Liu, D. Wu, Q. Zhang, Y. Li, Q. Qin, J. Li, Z. Zhu, Y. Cai, D. Wu, J. Tang, H. Qian, Y. Wang, H. Wu, *Science* **2023**, *381*, 1205.

[2] Z. Gao, X. Ju, H. Zhang, X. Liu, H. Chen, W. Li, H. Zhang, L. Liang, H. Cao, *Adv. Funct. Mater.* **2023**, 2305959.

[3] M. Pei, Y. Zhu, S. Liu, H. Cui, Y. Li, Y. Yan, Y. Li, C. Wan, Q. Wan, *Adv. Mater.* **2023**, *35*, 230560.

[4] H. Zhang, P. Qiu, Y. Lu, X. Ju, D. Chi, K. S. Yew, M. Zhu, S. Wang, R. Wei, W. Hu, *ACS Sens.* **2023**, *8*, 3873.

[5] J. Jiang, W. Hu, D. Xie, J. Yang, J. He, Y. Gao, Q. Wan, *Nanoscale* **2019**, *11*, 1360.

[6] X. Lin, et al., *Int. J. Extrem. Manuf.* **2024**, *6*, 032011.

[7] Y. Wei, et al., *Nano Energy* **2024**, *126*, 109622.

[8] J. Ji, Z. Wang, F. Zhang, B. Wang, Y. Niu, X. Jiang, Z. Qiao, T. Ren, W. Zhang, S. Sang, Z. Cheng, Q. Sun, *InfoMat* **2023**, *5*, e12478.

[9] M. Lukoševičius, H. Jaeger, *Computer science review* **2009**, *3*, 127-149.

[10] G. Tanaka, T. Yamane, J. B. Héroux, R. Nakane, N. Kanazawa, S. Takeda, H. Numata, D. Nakano, A. Hirose, *Neural Networks* **2019**, *115*, 100-123.

[11] M. Cucchi, S. Abreu, G. Ciccone, D. Brunner, H. Kleemann, *Neuromorph. Comput. Eng.* **2022**, *2*, 032002.

[12] K. Nakajima, *Japanese Journal of Applied Physics* **2020**, *59*, 060501.

[13] J. D. Caldwell, I. Aharonovich, G. Cassabois, J. H. Edgar, B. Gil, D. N. Basov, *Nat. Rev. Mater.* **2019**, *4*, 552.

[14] A. Pakdel, Y. Bando, D. Golberg, *Chem. Soc. Rev.* **2014**, *43*, 934.

[15] S. Angizi, S. A. A. Alem, M. Hasanzadeh Azar, F. Shayeganfar, M. I. Manning, A. Hatamie,A. Pakdel, A. Simchi, *Prog. Mater. Sci.* **2022**, *124*, 100884.

[16] M. Lanza, A. Sebastian, W. D. Lu, M. Le Gallo, M.-F. Chang, D. Akinwande, F. M. Puglisi, H. N. Alshareef, M. Liu, J. B. Roldan, *Science* **2022**, *376*, 1066.

[17] K. Watanabe, T. Taniguchi, H. Kanda, *Nat. Mater.* **2004**, *3*, 404.

[18] Q. Cai, D. Scullion, W. Gan, A. Falin, S. Zhang, K. Watanabe, T. Taniguchi, Y. Chen, E. J. G. Santos, L. H. Li, *Sci Adv* **2019**, *5*, eaav0129.

[19] L. H. Li, J. Cervenka, K. Watanabe, T. Taniguchi, Y. Chen, *ACS Nano* **2014**, *8*, 1457.

[20] J. Wu, W. Q. Han, W. Walukiewicz, J. W. Ager, W. Shan, E. E. Haller, A. Zettl, *Nano Lett.* **2004**, *4*, 647.

[21] K. A. Aissa, N. Semmar, A. Achour, Q. Simon, A. Petit, J. Camus, C. Boulmer-Leborgne, M. A. Djouadi, *J. Phys. D Appl. Phys.* **2014**, *47*, 355303.

[22] J. Lin, R. Y. Tay, H. Li, L. Jing, S. H. Tsang, H. Wang, M. Zhu, D. G. McCulloch, E. H. T. Teo, *Nanoscale* **2018**, *10*, 16243.

[23] D. M. Stewart, R. J. Lad, *Phys. Status Solidi B Basic Res.* **2018**, *255*, 1700458.

[24] J. Sun, C. Lu, Y. Song, Q. Ji, X. Song, Q. Li, Y. Zhang, L. Zhang, J. Kong, Z. Liu, *Chem. Soc. Rev.* **2018**, *47*, 4242.

[25] M. Zhu, H. Zhang, Z. Du, C. Liu, *Ceram. Int.* **2019**, *45*, 22324.

[26] S. S. Chng, M. Zhu, Z. Du, X. Z. Wang, M. Whiteside, Z. K. Ng, M. Shakerzadeh, S. H. Tsang, E. Teo, *J. Mater. Chem. C* **2020**, *45*, 22324.

[27] C. Du, F. Cai, M. A. Zidan, W. Ma, S. H. Lee, W. D. Lu, *Nat. Commun.* **2017**, *8*, 2204.

[28] L. Sun, Z. Wang, J. Jiang, Y. Kim, B. Joo, S. Zheng, S. Lee, W. J. Yu, B.-S. Kong, H. Yang, *Sci. Adv.* **2021**, *7*, eabg1455.

[29] L. Appeltant, M. C. Soriano, G. Van der Sande, J. Danckaert, S. Massar, J. Dambre, B. Schrauwen, C. R. Mirasso, I. Fischer, *Nat. Commun.* **2011**, *2*, 468.

[30] P. Yao, H. Wu, B. Gao, J. Tang, Q. Zhang, W. Zhang, J. J. Yang, H. Qian, *Nature* **2020**, *577*, 641.

[31] R. Midya, Z. Wang, S. Asapu, X. Zhang, M. Rao, W. Song, Y. Zhuo, N. Upadhyay, Q. Xia, J. J. Yang, *Adv. Intell. Syst.* **2019**, *1*, 1900084.

[32] S. S. Chng, M. Zhu, J. Wu, X. Wang, Z. K. Ng, K. Zhang, C. Liu, M. Shakerzadeh, S. Tsang, E. H. T. Teo, *J. Mater. Chem. C* **2020**, *8*, 4421.

[33] B. Zhang, B. Chen, J. Wu, S. Hao, G. Yang, X. Cao, L. Jing, M. Zhu, S. H. Tsang, E. H. T. Teo, Y. Huang, *Small* **2017**, *13*, 1603411.

[34] H. Zhang, X. Ju, K. S. Yew, D. S. Ang, *ACS Appl. Mater. Interfaces* **2020**, *12*, 1036.

[35] M. D'Esposito, B. R. Postle, *Annu. Rev. Psychol.* **2015**, *66*, 115.

[36] F.-S. Yang, M. Li, M.-P. Lee, I.-Y. Ho, J.-Y. Chen, H. Ling, Y. Li, J.-K. Chang, S.-H. Yang, Y.-M. Chang, K.-C. Lee, Y.-C. Chou, C.-H. Ho, W. Li, C.-H. Lien, Y.-F. Lin, *Nat. Commun.* **2020**, *11*, 2972.

[37] S. Seo, B.-S. Kang, J.-J. Lee, H.-J. Ryu, S. Kim, H. Kim, S. Oh, J. Shim, K. Heo, S. Oh, J.-H. Park, *Nat. Commun.* **2020**, *11*, 3936.

[38] P.-Y. Chen, X. Peng, S. Yu, In *2017 IEEE International Electron Devices Meeting (IEDM)*, IEEE, **2017**, pp. 6.1.1-6.1.4.

[39] S. Kim, B. Choi, M. Lim, J. Yoon, J. Lee, H.-D. Kim, S.-J. Choi, *ACS Nano* **2017**, *11*, 2814.

[40] S. Park, A. Sheri, J. Kim, J. Noh, J. Jang, M. Jeon, B. Lee, B. R. Lee, B. H. Lee, H. J. Hwang, *IEEE International Electron Devices Meeting (IEDM)* **2013**, 25-6.

[41] J. Woo, K. Moon, J. Song, S. Lee, M. Kwak, J. Park, H. Hwang, *IEEE Electron Device Lett.* **2016**, *37*, 994-997.

[42] D. Nishioka, T. Tsuchiya, T. Higuchi, K. Terabe, *Neuromorph. Comput. Eng.* **2023**, *3*, 034008.

[43] P. Apsangi, H. Barnaby, M. Kozicki, Y. Gonzalez-Velo, J. Taggart, *Neuromorph. Comput. Eng.* **2022**, *2*, 021002.

[44] C. J. Wan, L. Q. Zhu, Y. H. Liu, P. Feng, Z. P. Liu, H. L. Cao, P. Xiao, Y. Shi, Q. Wan, *Adv. Mater.* **2016**, *28*, 3557.

[45] R. S. Zucker, W. G. Regehr, *Annu. Rev. Physiol.* **2002**, *64*, 355.

[46] X. Ju, D. S. Ang, *IEEE Electron Device Lett.* **2022**, *43*, 793.

[47] H. Markram, A. Gupta, A. Uziel, Y. Wang, M. Tsodyks, *Neurobiol. Learn. Mem.* **1998**, *70*, 101.

[48] P. Yao, H. Wu, B. Gao, J. Tang, Q. Zhang, W. Zhang, J. J. Yang, H. Qian, *Nature* **2020**, *577*, 641.

[49] G. Zhang, J. Qin, Y. Zhang, G. Gong, Z. Xiong, X. Ma, Z. Lv, Y. Zhou, S. Han, *Adv. Funct. Mater.* **2023**, *33*, 2302929.

[50] Z. Qi, L. Mi, H. Qian, W. Zheng, Y. Guo, Y. Chai, *Adv. Funct. Mater.* **2023**, *33*, 2306149.

[51] Y. Zhong, J. Tang, X. Li, X. Liang, Z. Liu, Y. Li, Y. Xi, P. Yao, Z. Hao, B. Gao, H. Qian, H. Wu, *Nat. Electron.* **2022**, *5*, 672.

[52] R. Legenstein, W. Maass, *Neural networks* **2007**, *20*, 323-334.

[53] H. Jaeger, *Short term memory in echo state networks* **2001**.

[54] X. Wu, S. Wang, W. Huang, Y. Dong, Z. Wang, W. Huang, *Nat. Commun.* **2023**, *14*, 468.

[55] W. Jiang, L. Chen, Zhou, K. Zhou, L. Li, Q. Fu, Y. Du, R. H. Liu, *Appl. Phys. Lett.* **2019**, *115*, 19.

[56] R. Midya, Z. Wang, S. Asapu, X. Zhang, M. Rao, W. Song, Y. Zhuo, N. Upadhyay, Q. Xia, J. J. Yang, *Adv. Intell. Syst.* **2019**, *1*, 1900084.

[57] C. Du, F. Cai, M.A. Zidan, W. Ma, S.H. Lee, W.D. Lu, *Nat. Commun.* **2017**, *8*, 2204.

[58] D. Nishioka, T. Tsuchiya, W. Namiki, M. Takayanagi, M. Imura, Y. Koide, T. Higuchi, K. Terabe, *Sci. Adv.* **2022**, *8*, 50.